

# Boosting Magnetoacoustic Coupling with Spin Current in Ferromagnet/Nonmagnet/Ferromagnet Multilayers

Shuting Cui<sup>#</sup>, Fa Chen<sup>#</sup>, Liyang Liao<sup>2</sup>, Rui Xiong<sup>3</sup>, Xiaofei Yang<sup>1</sup>, Yoshichika Otani<sup>2, 4, 5</sup>, Yue Zhang<sup>1, 6\*</sup>, Wei Luo<sup>1\*</sup>

<sup>1</sup>School of Integrated Circuits, Huazhong University of Science and Technology, Wuhan, 430074, China

<sup>2</sup>Institute for Solid State Physics, University of Tokyo, Kashiwa 277-8581, Japan.

<sup>3</sup>School of Physics and Technology, Wuhan University, Wuhan 430072, China

<sup>4</sup>Center for emergent Matter Science, RiKen, Wako, Saitama 351-0198, Japan.

<sup>5</sup>Trans-scale Quantum Science institute, University of Tokyo, Tokyo 113-8654, Japan.

<sup>6</sup>Songshan Lake Materials Laboratory, Dongguan, Guangdong 523808, China

<sup>#</sup>Shuting Cui and Fa Chen contributed equally to this work.

\*Corresponding author: [yue-zhang@hust.edu.cn](mailto:yue-zhang@hust.edu.cn) (Yue Zhang); [luowei@hust.edu.cn](mailto:luowei@hust.edu.cn) (Wei Luo)

Surface acoustic wave (SAW) induced ferromagnetic resonance (FMR) is the critical principle of novel magnetoacoustic coupling devices, such as SAW non-reciprocal propagation and SAW-driven spin pumping. However, the enhancement of magnetoacoustic coupling is constrained by the attenuation of strain in magnetic thin films and the intricate manufacturing process of high-frequency SAW devices. This paper presents the observation of a pronounced enhancement in SAW-induced FMR within a ferromagnet/nonmagnet/ferromagnet (FM/NM/FM) multilayer structure deposited on a LiNbO<sub>3</sub> piezoelectric substrate. This enhancement is driven by spin current transmission, facilitated by the non-parallel alignment of magnetizations between the two FM layers. The increased FMR response is evidenced by an elevated absorption of SAW energy by the magnetic layer, signifying improved magnetoacoustic coupling. This finding opens new avenues for advancing magnetoacoustic coupling devices, providing a pathway to enhanced control and functionality in applications that leverage magnetoacoustic interactions.

## INTRODUCTION

The interaction between spin and magnetic moments at the interfaces of ferromagnetic (FM) and non-magnetic (NM) multilayer structures forms the foundation for the spintronic effect central to modern magnetic technologies. In these structures, the ability to control electron spins allows for phenomena such as giant magnetoresistance (GMR) and tunneling magnetoresistance<sup>1-4</sup>, spin pumping<sup>5</sup>, spin-transfer torque (STT)<sup>6,7</sup>, and spin-orbit torque (SOT)<sup>8,9</sup>.

In recent years, surface acoustic waves (SAWs) have emerged as a promising tool for controlling

spintronic effects in FM/NM multilayer systems<sup>10,11</sup>. SAWs are mechanical waves that propagate along the surface of a piezoelectric substrate and induce periodic strain fields, which can couple with magnetic layers through magnetoelastic interactions. The SAW-driven magnetization dynamics presents a highly energy-efficient and localized method for controlling magnetization, eliminating the need for large external magnetic fields or electric currents. The typical example is the SAW-induced FMR<sup>12,13</sup>, where the magnetization in the FM layer precesses in response to the strain oscillations from the SAWs. Based on the SAW-induced FMR, SAWs can further enhance spintronic effects in FM/NM multilayers, such as spin pumping,

by exciting magnetization precession in an FM layer, which injects spin currents into an adjacent NM layer<sup>14</sup>.

Despite these advances, SAW-driven magnetoacoustic coupling is often relatively weak at low frequency, especially in the case of Rayleigh-type SAWs. As most of the Rayleigh-type SAW energy is confined to the near-surface region of the substrate, and the interaction between the strain field and the magnetic thin film, particularly those positioned close to the substrate, tends to diminish with increasing film thickness. This energy confinement limits the magnetoacoustic coupling in thicker films or multilayer systems. To address this, strong magnetoacoustic coupling was achieved in a 6.6 GHz acoustic cavity by using the shear horizontal (SH) wave, which can penetrate deeper into the film and produce more effective magnetoelastic interactions<sup>15</sup>. However, SAW devices above 2 GHz require more complex fabrication processes, making the enhancement of magnetoacoustic coupling challenging in practical applications. Therefore, how to effectively enhance the coupling between SAW and magnetic moments remains an open question, which is significant for developing SAW-driven spintronics devices with strong signals.

In addition to utilizing various types of SAW, another potential approach to enhancing magnetoacoustic coupling is modifying FM/NM systems to introduce coupling among more elements, such as SAW, magnetic moments, and spin currents. Notably, in this work, we observed that in FM/NM/FM multilayer systems, even though the magnetoacoustic interaction is confined at the bottom FM layer near the substrate interface with very weak magnetic precession under SAWs, the magnetoacoustic coupling can still be significantly enhanced based on the propagation of spin currents excited by the magnetic precession.

Our research introduces a novel approach to effectively enhance the coupled magnetization precession dynamics in two FM layers via the spin current generated by acoustic spin pumping. This previously unexplored mechanism provides a new way to control coupling between acoustic waves and

magnetic moments, with broad implications for magnetic sensing, energy-efficient memory devices, and spintronic technologies that utilize SAW to manipulate magnetic states.

## RESULTS

### 1. Experimental setup and core concept

The core concept of the paper centers around the coupling between magnetization dynamics and SAWs mediated by spin currents in a FM/Cu/FM structure on a piezoelectric LiNbO<sub>3</sub> substrate. Here Cu is famous for its long diffusion length of spin current<sup>16,17</sup>.

The device structure is shown in Fig. 1(a). The interdigital transducers (IDTs) made of Al are fabricated on the surface of the LiNbO<sub>3</sub> substrate to generate Rayleigh-type SAWs with a central frequency of 1.6 GHz. In the intermediate region between the two IDTs, a composite FM<sub>1</sub>/Cu/FM<sub>2</sub> thin film is deposited using direct current (DC) magnetron sputtering. The microscopic photograph of the device is shown in Fig. 1(b). The Rayleigh-type SAW initiates magnetization precession in the bottom ferromagnetic layer, generating a spin current that traverses the intermediate Cu layer to interact with the magnetic moments in the upper FM layer. When the magnetizations of the two FM layers are non-parallel, this spin current also induces precession in the upper FM layer. This, in turn, produces a reciprocal spin current that reinforces the magnetization precession in the bottom layer, leading to enhanced absorption of SAW energy [Fig. 1(c)].

In the present study, Co and NiFe were used as the bottom and top FM layers, respectively. Compared to Co, NiFe exhibits a negligible magnetoelastic coupling coefficient and much weaker damping. This ensures that the magnetoacoustic coupling is predominantly concentrated in the bottom layer. On the other hand, the backward spin current generated from the upper NiFe layer is stronger than the forward spin current emitted from the bottom Co layer, effectively enhancing the magnetization precession in the bottom Co layer.

Both of the Co and NiFe have a thickness of 20 nm. The thickness of the NM layer composed of Cu is 8 nm or less. A vector network analyzer (VNA) is connected to the IDTs to excite the Rayleigh SAW. The variation of the transmission parameter  $S_{21}$  is measured as a function of magnetic field strength under different in-plane magnetic field orientations. Without a  $FM_1/Cu/FM_2$  thin film, the  $S_{21}$  spectrum exhibits the maximum value near 1.6 GHz [Fig. 1(d)], which is consistent with the expected maximum absorption of SAW based on the size of the IDTs.

The experimental findings demonstrate that the absorption of SAW energy is greatly enhanced by the spin current transfer between the two FM layers. Notably, when the spin current is interrupted (for example, by removing the Cu layer or intersecting additional layer for inhibiting the spin current propagation), this enhanced absorption of SAW energy becomes clearly depressed. Interestingly, even when the SAW-induced magnetic precession in the lower FM layer is weak due to its strong damping, the assistance of the spin current considerably enhances the SAW absorption.

## 2. Orientation-dependent $S_{21}$ and magnetic hysteresis loops (M-H)

Fig. 2 demonstrates the relationship between  $S_{21}$  and magnetic field strength for four structures: Co(20)/Cu(8)/NiFe(20)/Pt(5), Co(20)/NiFe(20)/Pt(5), Co(20)/Cu(8)/Pt(5), and NiFe(20)/Cu(8)/Co(20)/Pt(5) under magnetic field orientations of  $\varphi_H = 0$  (parallel to the SAW propagation) and  $\varphi_H = \pi/2$  (perpendicular to the SAW propagation). The results shown in Fig. 2(a) ~ (c) reveal that for Co(20)/Cu(8)/NiFe(20)/Pt(5), the  $S_{21}$  change is weak when  $\varphi_H = 0$ , but significantly enhanced when  $\varphi_H = \pi/2$ . However, in the other two structures,  $S_{21}$  change remains weak for both magnetic field orientations. As shown in the inset of Fig. 2(a), the polar plot of  $S_{21}$  change measured at different magnetic field angles verified the most significant absorption of SAW at  $\varphi_H = \pi/2$  and  $\varphi_H = 3\pi/2$ . This is different from the typical angular dependence of the conventional magnetoelastic coupling, which satisfies  $\sin^2(2\varphi_H)$  with

the strongest SAW absorption at  $\varphi_H = (n + 1/2)\pi/2$  with  $n = 0, 1, 2,$  and  $3$ <sup>12,13</sup>.

The comparison of the results in Fig.2 (a) ~ (d) indicates that the magnetic precession excited solely by SAW is very weak, and the Cu layer also plays a very crucial role in the significant enhancement of SAW absorption with the intersection of Cu between the top and bottom FM layers [Fig. 2(a) and (b)]. Fig. 2(c) demonstrates that, in the case of magnetoacoustic coupling involving only the Co layer, SAW absorption is weak, with a value of just 0.02 dB. Additionally, the absorption of SAW is negligible for both magnetic field orientations when the sequence of NiFe and Co is swapped [Fig. 2(d)]. In this case, the magnetoelastic coupling constant of the bottom NiFe substrate and the penetration of SAW into the upper Co layer are both negligible [Fig. 2(d) and its inset].

Therefore, the significant enhancement of SAW absorption shown in Fig. 2(a) results from the combined effects of spin current and magnetoacoustic coupling. Under the SAW, the magnetization precession at the bottom Co layer was excited, which generates spin current that transmits through the Cu layer and feeds back from the NiFe layer. As a result, the spin current significantly enhances the coupling between the SAW and the magnetization precession in Co, thereby increasing SAW absorption.

The interaction between spin current and magnetic moments is proportional to the cross production between spin polarization and magnetic moment, and is maximum at an angle of  $\pi/2$  between them. Here the spin polarization is collinear with the magnetization at the equilibrium state. We measured the magnetic hysteresis loops (M-H) of the Co(20)/Cu(8)/Pt(5) and Cu(8)/NiFe(20)/Pt(5) systems by using the vibrating sample magnetometer (VSM), both of which exhibit clear uniaxial anisotropy [Fig. 2(e) and (f)]. The easy axes of the NiFe and Co layers are oriented at a  $\pi/2$  angle to each other, and the coercivity of NiFe is significantly smaller. These differences in magnetic properties between NiFe and Co lead to a non-collinear alignment of the magnetic moments of the two layers

under a small applied field, with an angle of  $\varphi_H = \pi/2$ . This strengthened the coupling between spin and magnetic moments, enhancing the magnetization precession that further strengthened the SAW absorption. It is also noted that the magnetic moments of the two layers are non-collinear within a small range of  $H$  near the origin at  $\varphi_H = 0$ . However, the SAW absorption due to pure magnetoelastic coupling at  $\varphi_H = 0$  is much weaker than at  $\varphi_H = \pi/2$  [Insets of Figs. 2(c)]. Consequently, the spin-current-induced enhancement of SAW absorption at  $\varphi_H = 0$  is significantly weaker than at  $\varphi_H = \pi/2$ .

It was observed that the enhanced  $S_{21}$  under a magnetic field, oriented perpendicular to the propagation of the Rayleigh-type SAW, occurs in magnetic films with a uniaxial anisotropy field aligned along the SAW propagation direction<sup>18</sup>. Although the bottom Co layer does indeed exhibit this sort of uniaxial anisotropy, this characteristic alone cannot account for our findings. The SAW absorption induced by uniaxial anisotropy typically aligns with general SAW absorption from magnetoelastic coupling, lacking the observed enhancement exceeding an order of magnitude.

To further verify the role of spin current, we investigated the influence of Cu thickness and the replacement of Cu with Pt of varying thickness in the middle layer on  $S_{21}$ . When the Cu thickness is below 2 nm,  $S_{21}$  significantly increases with increasing Cu thickness [Fig.3 (b)]. However, when the Cu thickness is between 2 nm and 8 nm,  $S_{21}$  stabilizes, which aligns with the long spin diffusion length of Cu. On the other hand, since the Ruderman–Kittel–Kasuya–Yosida (RKKY) coupling between the two FM layers is generally negligible due to the Cu layer being significantly thicker than 2 nm, the SAW-triggered magnetization dynamics observed in this study fundamentally differ from the recently reported magnetic dynamics induced by RKKY coupling<sup>19–21</sup>. Fig.3 (d) demonstrates the results of substituting Cu with Pt. Experiments indicate that replacing Cu with Pt of at least 3 nm in thickness also significantly reduces  $S_{21}$ . This effect arises from the obstruction of spin current transmission in Pt, further confirming that the transmission of spin current through the intermediate

layer plays a crucial role in enhancing  $S_{21}$ .

### 3. Calculate the role of spin current in magnetoacoustic coupling

In order to theoretically verify the role of spin current in enhancing SAW absorption, we calculated the spin dynamics in the FM/NM/FM trilayer based on the Landau-Lifshitz-Gilbert (LLG) equations with the damping-like torque from the spin current<sup>22</sup>:

$$\frac{\partial \mathbf{m}}{\partial t} = -\gamma \mathbf{m} \times \mathbf{H}_{\text{eff}} + \alpha \mathbf{m} \times \frac{\partial \mathbf{m}}{\partial t} + c \mathbf{m} \times (\mathbf{m} \times \mathbf{m}') \quad (1)$$

$$\frac{\partial \mathbf{m}'}{\partial t} = -\gamma' \mathbf{m}' \times \mathbf{H}'_{\text{eff}} + \alpha' \mathbf{m}' \times \frac{\partial \mathbf{m}'}{\partial t} - c' \mathbf{m}' \times (\mathbf{m}' \times \mathbf{m}) \quad (2)$$

where  $\mathbf{m}$  and  $\mathbf{H}_{\text{eff}}$  are the magnetization and effective magnetic field of the upper FM layer, respectively. And the relevant parameters of the bottom FM layer are shown by the symbol with the apostrophe in the top right corner.  $\alpha$  and  $\gamma$  are the Gilbert damping coefficient and gyromagnetic ratio of the upper FM layer, respectively. Here,  $c$  is a coefficient characterizing the strength of the damping-like torque. The opposite signs for the two damping-like torques in Eqs. (1) and (2) indicate opposite propagation directions of spin currents. We estimated the expression of  $c$  as  $c = \Delta\alpha(H + 2\pi M_S)\gamma$  from the relationship between the intrinsic damping of the FM layer and the spin current induced damping change  $\Delta\alpha$  due to spin pumping [Supplementary Material I]. The equilibrium magnetization orientation is along the 3-axis of the (1,2,3) coordinate system, and the magnetization angle of the upper FM layer is  $\varphi_M$ . The 3'-axis of the (1',2',3') coordinate system is the equilibrium magnetization orientation, and the magnetization angle of the bottom FM layer is  $\varphi'_M$  [Fig. 4(a)].  $\phi = \varphi'_M - \varphi_M$  is the angle between the magnetizations of two FM layers.

For the Rayleigh-type SAW, we only consider the longitudinal strain  $\varepsilon_{xx}$  [Supplementary Material II]. The free energy density of the upper FM layer is

$$G = -\mathbf{H} \cdot \mathbf{m} + B_d m_z^2 + B_u (\mathbf{m} \cdot \mathbf{u})^2 + b_1 \varepsilon_{xx} m_x^2 - D_s \frac{\partial^2 \mathbf{m}}{\partial x^2} \cdot \mathbf{m} \quad (3)$$

where  $b_1$  is the magnetoelastic coupling constant of the upper FM layer;  $\mathbf{H}$  is the external magnetic field.  $B_d$  and  $B_u$  represent the shape anisotropy and uniaxial

anisotropy, respectively.  $\mathbf{u}$  is the direction vector of uniaxial anisotropy.  $D_s$  is the exchange stiffness constant. The effective magnetic field derived from the free-enthalpy density is  $\mathbf{H}_{\text{eff}} = -\nabla_{\mathbf{m}} G$ . Similarly, the effective magnetic field of the bottom FM layer is denoted as  $\mathbf{H}'_{\text{eff}} = -\nabla_{\mathbf{m}'} G'$ ,  $G'$  is the free-enthalpy density of the bottom FM layer.

The plane-wave approximation is made for magnetization  $m_i = m_i^0 e^{j(kx - \omega t)}$  ( $i=1,2$ ),  $m_3 \approx 1$ .  $k$  and  $\omega$  are the angular frequency and wave vector, respectively. Substituting the effective magnetic field into the LLG equations, we derived the magnetization equation of the FM/NM/FM trilayer

$$\mathbf{M} = \boldsymbol{\chi} \mathbf{h} \quad (4)$$

where  $\boldsymbol{\chi} = \mathbf{D}^{-1}$ ,  $\mathbf{M} = [M_s m_1 \quad M_s m_2 \quad M'_s m'_1 \quad M'_s m'_2]^T$ .  $M_s$  and  $M'_s$  are the saturation magnetization of the upper and bottom FM layers, respectively.  $\mathbf{D}$  is the coefficient matrix [Supplementary Material III].  $\mathbf{h}$  represents the effective magnetic field derived from spin current and strain, denoted as

$$\mathbf{h} = \begin{bmatrix} \frac{cM'_s}{\gamma M'_s} \sin \phi \\ 2b_1 \varepsilon_{xx} \sin \phi_M \cos \phi_M \\ \frac{c'M_s}{\gamma' M_s} \sin \phi \\ 2b'_1 \varepsilon_{xx} \sin \phi'_M \cos \phi'_M \end{bmatrix} \quad (5)$$

The power absorption of SAW by the FM/NM/FM trilayer is expressed as

$$P_{\text{abs}} \propto \int_0^\lambda \mathbf{h}^T \boldsymbol{\chi} \mathbf{h} dx \quad (6)$$

where  $\lambda$  is the wave length of SAW.

When  $\phi_H = \pi/2$ , the absorption of SAW by Co/Cu/NiFe is calculated. The easy axis of NiFe is along the  $y$ -axis,  $B_u = 1$  mT. The easy axis of Co is along the  $x$ -axis direction,  $B_u = 8$  mT. While the magnetoelastic coefficient of NiFe is disregarded, that of Co is  $10 \text{ T}^{21}$ . The exchange stiffnesses of NiFe and Co are  $1.43 \times 10^{-17} \text{ T} \cdot \text{m}^2$  and  $1.59 \times 10^{-17} \text{ T} \cdot \text{m}^2$ , respectively<sup>23,24</sup>. The SAW frequency is 1.6 GHz, the wavelength  $\lambda$  is 2.4  $\mu\text{m}$ , and  $\varepsilon_{xx} = 10^{-6}$ . The saturation magnetizations of NiFe and Co are  $7.69 \times 10^5 \text{ A/m}$  and  $9.7 \times 10^5 \text{ A/m}$ , respectively. The gyromagnetic ratio  $\gamma = \gamma' = 1.76 \times 10^{11} (\text{T} \cdot \text{s})^{-1}$ . The Gilbert damping of Co and NiFe are 0.2 and 0.002, respectively. Here we considered the modification of SAW on the damping

coefficient [Supplementary Material I]. The interplay of the uniaxial anisotropic field and the magnetic elastic field causes little change in SAW energy when  $c = 0$ . The influence of spin current enhances the absorption of SAW when  $c = \Delta\alpha(H + 2\pi M_s)\gamma$  [Fig. 4(b)]. This is consistent well with the experimental results. Additionally, we also estimated the amplitude of the density of spin current ejected from NiFe and Co by using the formula:

$$J_s^{\text{NiFe}} / J_s^{\text{Co}} = \frac{M_s^{\text{NiFe}} \Delta\alpha^{\text{NiFe}} (\mathbf{M}^{\text{NiFe}} \times d\mathbf{M}^{\text{NiFe}}/dt)^{\text{Amp}}}{M_s^{\text{Co}} \Delta\alpha^{\text{Co}} (\mathbf{M}^{\text{Co}} \times d\mathbf{M}^{\text{Co}}/dt)^{\text{Amp}}} \quad (7)$$

where superscript *Amp* indicates the amplitude. Obviously, the spin current density of NiFe is significantly larger than that of Co [Fig. 4(b)], which verifies that the significant enhancement of the SAW absorption originates from the backward spin current from the magnetization precession in NiFe.

## DISCUSSION AND SUMMARY

The enhanced SAW absorption driven by spin current is not directly related to magnetoelastic coupling. Instead, it arises from the reduction of the effective damping coefficient in the bottom Co layer, caused by the strong spin current ejected from the upper NiFe. It is also important to notice that the enhancement of magnetization precession in Co does not violate angular momentum conservation, as the enhanced absorption of SAW results from an expansion in the amplitude of magnetization precession due to modified damping, rather than a change in the mean value from a variation in net angular momentum.

In summary, this study reveals the spin current assisted enhancement of coupling between SAW and magnetic precession in a multilayer FM/Cu/FM structure on a piezoelectric LiNbO<sub>3</sub> substrate. We demonstrate the substantial contribution of spin current to enhancing SAW absorption, which is relevant to the noncollinear alignments of the magnetization of the two FM layers.

These findings not only deepen our understanding of the interaction between spin current and SAW but also open new avenues for the design of acoustic devices based on the manipulation of spin current. By optimizing the material selection of multilayer

structures, it is possible to achieve more efficient magnetoacoustic coupling, laying the groundwork for the development of novel information storage and processing technologies, showcasing their potential application prospects.

## MATERIALS AND METHODS

Using electron beam evaporation, a 72 nm Al electrode with an electrode width of 600 nm and a separation of 600 nm from neighboring electrodes was created on 128°-YX LiNbO<sub>3</sub>. The IDT is made up of 25 pairs of electrodes. Two IDTs create a SAW delay line on 128°-YX LiNbO<sub>3</sub> with a delay distance of 1440 μm. Samples were fabricated on 128°-YX LiNbO<sub>3</sub> substrates using ultra-high vacuum DC magnetron sputtering. A hard mask was employed to define the magnetic film size as

375 μm × 1500 μm, and Co(20)/Cu(8)/NiFe(20)/Pt(5) stacks were deposited on the substrate with IDTs at room temperature, under a base pressure better than 1 × 10<sup>-7</sup> torr. (numbers are nominal thicknesses in nanometres). Ar gas was used during the sputtering process. Co, Cu NiFe and Pt layers were deposited at a working pressure of 0.3 Pa with the sputtering rate of 25.1 s/nm, 8.2 s/nm, 16 s/nm and 7.6 s/nm, respectively.

A vector network analyzer (Keysight E5071C) was used to apply and detect SAW signals. An electromagnet is placed under the sample to provide an in-plane magnetic field. Magnetic properties were measured by vibrating sample magnetometer (Quantum Design PPMS).

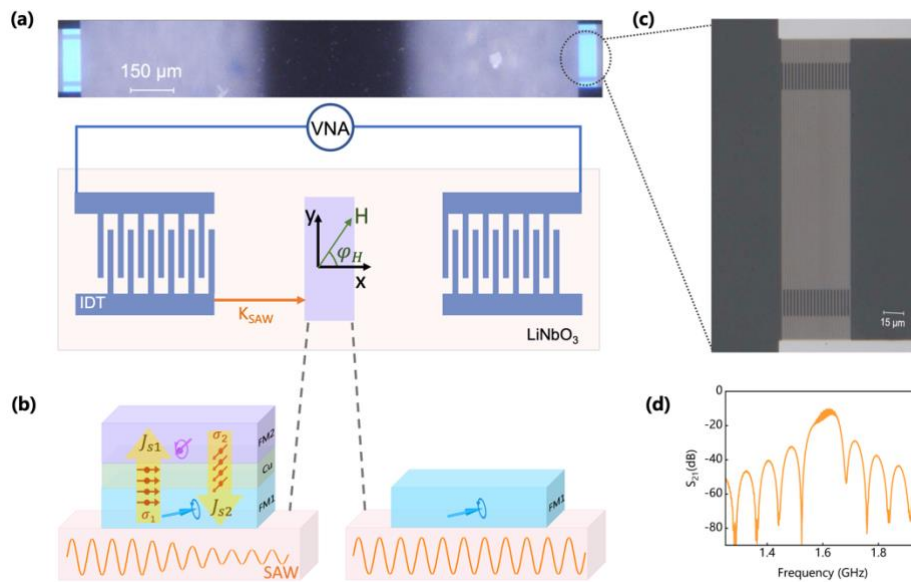


Figure. 1 (a) Schematic representation of the device with microscopic image, featuring a pair of IDTs on a LiNbO<sub>3</sub> substrate, with a magnetic thin film positioned at the center of the delay line, measured using a VNA. (b) Illustration of the operational mechanism, depicting two FM layers with magnetic moments oriented in different directions, separated by a Cu layer. The spin current facilitates transmission and enhancement between the top and bottom FM layers, resulting in significant absorption of SAW signals. A single FM layer exhibits weaker SAW absorption. (c) Microscopic image of the basic IDT configuration. (d) Measured S<sub>21</sub> of Rayleigh-type SAW, centered at a frequency of 1.6 GHz.

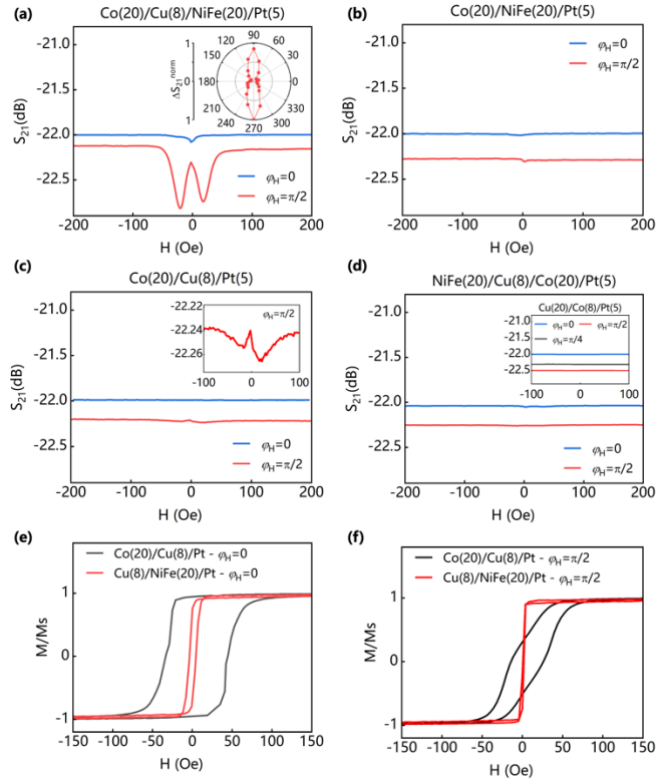


Figure. 2 The  $S_{21}$  measured by the VNA varies with  $\varphi_H = 0$  and  $\varphi_H = \pi/2$ , for the following film structures: (a) Co(20)/Cu(8)/NiFe(20)/Pt(5), (b) Co(20)/NiFe(20)/Pt(5), (c) Co(20)/Cu(8)/Pt(5) and (d) NiFe(20)/Cu(8)/Co(20)/Pt(5). The inset in (a) shows the normalized  $S_{21}$  variations of Co(20)/Cu(8)/NiFe(20)/Pt(5) at various magnetic field angles. The inset in (c) is the result of y-axis magnification at  $\varphi_H = \pi/2$ . The variation of  $S_{21}$  with  $\varphi_H$  for Cu(20)/Co(8)/Pt(5) is shown in the inset of (d). (e) and (f) show the VSM results for Co(20)/Cu(8)/Pt(5) and Cu(8)/NiFe(20)/Pt(5) at  $\varphi_H = 0$  and  $\varphi_H = \pi/2$ .

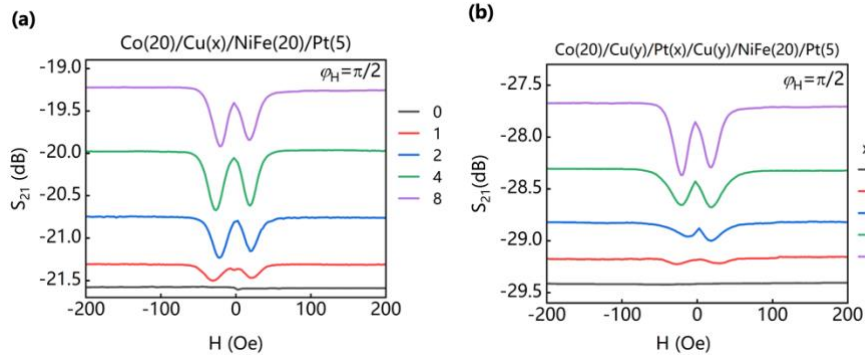


Figure. 3 (a)  $S_{21}$  variation for  $\varphi_H = \pi/2$  with Cu thickness between Co and NiFe varying from 0 to 8 nm, respectively. (b)  $S_{21}$  results with the Cu spacer layer replaced by Pt at varying thicknesses.

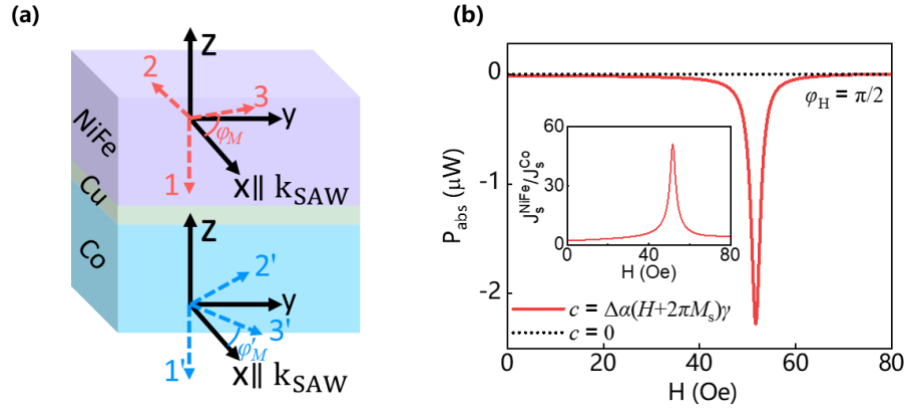


Figure 4 (a) Coordinate systems employed in calculations. The top and bottom layers establish coordinate systems with the magnetic moment direction aligned along the 3-axis and 3'-axis, with an angle of  $\varphi_M$  between the 3-axis and the x-axis, and an angle of  $\varphi'_M$  between the 3'-axis and the x-axis. (b) Calculated absorption intensity based on the specified conditions for  $c = \Delta\alpha(H + 2\pi M_s)\gamma$  and  $c = 0$ . The inset in (b) is the ratio of the amplitude of the density of the spin current ejected from NiFe and Co in the case of  $c = \Delta\alpha(H + 2\pi M_s)\gamma$ .

### Acknowledgements:

This work was supported by the National Key Research and Development Program of China (Grant No. 2022YFE0103300), and the National Natural Science Foundation of China (Grant No. U2141236 and 12227806), and the open research fund of Songshan Lake Materials Laboratory (Grant No. 2023SLABFN26).

### Reference

1. Baibich, M. N. *et al.* Giant magnetoresistance of (001)Fe/(001)Cr magnetic superlattices. *Phys. Rev. Lett.* **61**, 2472–2475 (1988).
2. Binasch, G., Grünberg, P., Saurenbach, F. & Zinn, W. Enhanced magnetoresistance in layered magnetic structures with antiferromagnetic interlayer exchange. *Phys. Rev. B* **39**, 4828–4830 (1989).
3. Miyazaki, T., Yaoi, T. & Ishio, S. Large magnetoresistance effect in 82Ni-Fe/Al-Al<sub>2</sub>O<sub>3</sub>/Co magnetic tunneling junction. *J. Magn. Magn. Mater.* **98**, L7 (1991).
4. Butler, W. H., Zhang, X. G., Schulthess, T. C. & MacLaren, J. M. Spin-dependent tunneling conductance of Fe/MgO/Fe sandwiches. *Phys. Rev. B* **63**, 544161–5441612 (2001).
5. Tserkovnyak, Y., Brataas, A. & Bauer, G. E. W. Enhanced Gilbert Damping in Thin Ferromagnetic Films. *Phys. Rev. Lett.* **88**, 117601 (2002).
6. Slonczewski, J. C. Current-driven excitation of magnetic multilayers. *J. Magn. Magn. Mater.* **159**, L1–L7 (1996).
7. Berger, L. Emission of spin waves by a magnetic multilayer traversed by a current. *Phys. Rev. B* **54**, 9353–9358 (1996).
8. Miron, I. M. *et al.* Perpendicular switching of a single ferromagnetic layer induced by in-plane current injection. *Nature* **476**, 189–193 (2011).
9. Liu, L. *et al.* Spin-torque switching with the giant spin hall effect of tantalum. *Science*. **336**, 555–558 (2012).
10. Yang, W. G. & Schmidt, H. Acoustic control of magnetism toward energy-efficient applications. *Appl. Phys. Rev.* **8**, 021304 (2021).
11. Puebla, J., Hwang, Y., Maekawa, S. & Otani, Y. Perspectives on spintronics with surface acoustic waves. *Appl.*

- Phys. Lett.* **120**, 220502 (2022).
12. Weiler, M. *et al.* Elastically driven ferromagnetic resonance in nickel thin films. *Phys. Rev. Lett.* **106**, 117601 (2011).
  13. Dreher, L. *et al.* Surface acoustic wave driven ferromagnetic resonance in nickel thin films: Theory and experiment. *Phys. Rev. B* **86**, 134415 (2012).
  14. Weiler, M. *et al.* Spin pumping with coherent elastic waves. *Phys. Rev. Lett.* **108**, 176601 (2012).
  15. Hwang, Y. *et al.* Strongly Coupled Spin Waves and Surface Acoustic Waves at Room Temperature. *Phys. Rev. Lett.* **132**, 56704 (2024).
  16. Kobayashi, D. *et al.* Spin Current Generation Using a Surface Acoustic Wave Generated via Spin-Rotation Coupling. *Phys. Rev. Lett.* **119**, 077202 (2017).
  17. Kimura, T., Sato, T. & Otani, Y. Temperature evolution of spin relaxation in a NiFe/Cu lateral spin valve. *Phys. Rev. Lett.* **100**, 066602 (2008).
  18. Chen, F. *et al.* Widen-dynamic-range surface acoustic wave magnetic sensors with high sensitivity. *J. Alloys Compd.* **980**, 173635 (2024).
  19. Chen, C. *et al.* Electrical Detection of Acoustic Antiferromagnetic Resonance in Compensated Synthetic Antiferromagnets. *Phys. Rev. Lett.* **133**, 56702 (2024).
  20. Küß, M. *et al.* Giant Surface Acoustic Wave Nonreciprocity with Low Magnetoacoustic Insertion Loss in CoFeB/Ru/CoFeB Synthetic Antiferromagnets. *ACS Appl. Electron. Mater.* **5**, 5103–5110 (2023).
  21. Zhou, Z. *et al.* Nonreciprocal transmission of surface acoustic waves induced by magnetoelastic coupling with an anti-magnetostrictive bilayer. *J. Appl. Phys.* **136**, 163901 (2024).
  22. Liu, L., Moriyama, T., Ralph, D. C. & Buhrman, R. A. Spin-torque ferromagnetic resonance induced by the spin Hall effect. *Phys. Rev. Lett.* **106**, 1–4 (2011).
  23. Eyrich, C. *et al.* Exchange stiffness in thin film Co alloys. *J. Appl. Phys.* **111**, 07C919 (2012).
  24. Strelkov, N. *et al.* Exchange stiffness reduction in Ta substituted NiFe alloys. *J. Phys. D: Appl. Phys.* **56**, 395004 (2023).